



EXPERIMENTAL COMPARISON AND MODELING OF DOUBLE AND TRIPLE CONCAVE SEISMIC ISOLATORS

G. Lomiento⁽¹⁾, A. Adzhemyan⁽²⁾, G. Benzoni⁽³⁾, A. F. Koscal⁽⁴⁾, A. Penaflor⁽⁵⁾, S. Pouryaghoobi-Anzabi⁽⁶⁾

⁽¹⁾ Assistant Professor, Cal Poly Pomona, glomiento@cpp.edu

⁽²⁾ Research assistant, Cal Poly Pomona, arsenadzhemyan@yandex.ru

⁽³⁾ Research Scientist, University of California San Diego, gbenzoni@eng.ucsd.edu

⁽⁴⁾ Research assistant, Cal Poly Pomona, afkoscal@cpp.edu

⁽⁵⁾ Research assistant, Cal Poly Pomona, apenaflor@cpp.edu

⁽⁶⁾ Research assistant, Cal Poly Pomona, soheilp@cpp.edu

Abstract

Friction isolators are among the most commonly used devices for the seismic isolation of buildings and bridges. The objective of this study is the assessment and comparison of double and triple concave friction isolators with theoretically equivalent performance under design seismic loads. Two full-scale isolators, one of each type, were manufactured, analyzed and tested under quasi-static and dynamic shake table test conditions. The two specimens have the same effective design stiffness and damping ratio, and were subjected to mono-directional and bi-directional sliding patterns.

The comparison addresses both the isolators' kinematics, including vertical displacement patterns, and friction behavior. A unified model for the two isolator types was developed and is discussed in terms of its accuracy and validity. The model is comprised of a kinematics component, accounting for the restoring forces produced by the concave sliding on multiple surfaces, and a friction component. The kinematics component is capable of capturing the sequential sliding on multiple surfaces in case of triple concave isolators. The friction component relies on an existing experimental friction model previously validated for single and double concave isolators, which was extended to triple concave sliding isolators. The friction model accounts for the effects of contact pressure, sliding velocity and heat degradation of the frictional property. The variability of the friction property for the two isolators is further discussed to identify and quantify variations from the nominal design parameters.

The use of mono-directional test results to predict and simulate bi-directional sliding is finally investigated and discussed. This analysis includes the assessment of commercial software models calibrated by means of standardized mono-directional tests and their ability to represent the experimentally observed bi-directional dynamic behavior.

Keywords: seismic isolation, double concave isolator, triple concave isolator, full-scale tests, friction model.



1. Introduction

Recent developments in base isolation have it emerging as one of the most effective methods for protecting infrastructure against high seismic loading. At the forefront of base isolation technology is the implementation of multi-surface concave friction pendulum system devices, including double friction pendulums (DFP) and triple friction pendulums (TFP). With the implementation of additional sliding surfaces, the TFP potentially offers advantages in areas of adaptability, as well as effectiveness in limiting displacements during very large earthquakes [1].

Experimentally validated models for DFP and, recently, TFP have been proposed and implemented in commercial structural analysis software. DFP predictive models include (Kumar Lomiento) which are able to predict the heat-induced friction degradation during mono- and bi-directional sliding motion. Mono-directional analytical models for TFP were proposed [1, 2, 3], and recently implemented into a Finite Element model [4]. These models are validated through experimental results, and capture sequential sliding at different displacement levels based on radii of curvature of sliding surfaces under the assumption of constant coefficient of friction. A model capable of capturing the TFP bi-directional behavior was recently proposed [5]. This model is validated through experimental testing and shows discrepancies mainly associated with: (i) variation of the coefficient of friction during sliding, (ii) nonsymmetrical sliding over upper and lower surfaces, and (iii) limited re-centering capabilities. These phenomena are also observed in DFP devices, but are more evident and harder to account for in TFPs due to the increased number of moving parts and sliding surfaces. Particularly, changes in the friction property at the contact surfaces might result in changes in the sequential sliding with distortion of the lateral force-displacement loop performance.

This study aims at comparing two DFP and TFP devices, which were designed to be equivalent, in terms of effective stiffness and damping property at the design level. The investigation objective is threefold: (i) identify major observed discrepancies in the experimental performance of the devices, (ii) develop an analytical model for TFP as an extension of DFP models, and (iii) verify the accuracy of commercial software numerical models for TFP, with detailed nonlinear Finite Element models calibrated with experimental data.

2. Experimental testing

The main properties of the DFP and TFP devices are presented in Fig. 1 and Table 1. The major sliding surfaces of the two devices have identical friction and dimensions. The top and bottom properties of the TFP sliding surfaces are identical. The TFP used in this study is capable of achieving three sliding regimes, compared to the single regime DFP's motion. The expected force-displacement loop of the two devices is compared in Fig. 2 at the maximum TFP displacement level of 628 mm. The three different sliding regimes of the TFP isolator involve simultaneous sliding on the inner surfaces, followed by sliding on the outer surfaces, and finally on the inner surfaces until the maximum level of displacement is reached.

The two seismic isolators are expected to have an equivalent force-displacement behavior at the design displacement level of 500 mm. The comparison is based on effective stiffness and damping ratio, based on the mono-directional behavior of the devices. A comparison between the expected effective parameters of DFP and TFP devices at different displacement levels is presented in Fig. 3. The main differences in the damping ratio between DFP and TFP isolators are due to the transition between sliding regimes.

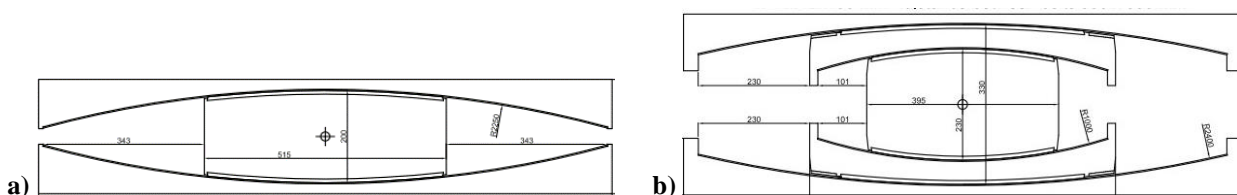


Fig. 1 – Section of a) DFP and b) TFP devices



Table 1 – Main design parameters of DFP and TFP devices

Parameter	DFP	TFP	Legend
N (kN)	6200	6200	Seismic vertical load
f_1 - f_4 (%)	6	6	Outer nominal friction coef.
f_2 - f_3 (%)	N/A	4	Inner nominal friction coef.
R_1 - R_4 (mm)	2250	2400	Outer radius of curvature
R_2 - R_3 (mm)	N/A	1000	Inner radius of curvature
d (mm)	± 650	± 628	Maximum horizontal displ.

Note: The TFP device has 3 sliding regimes: (i) Regime I: sliding on inner surfaces, (ii) Regime II: sliding on outer surfaces, (iii) Regime III: sliding on inner surfaces. The activation of Regime III follows the impact of the outer sliders with the retaining ring, at a theoretical displacement of 485 mm.

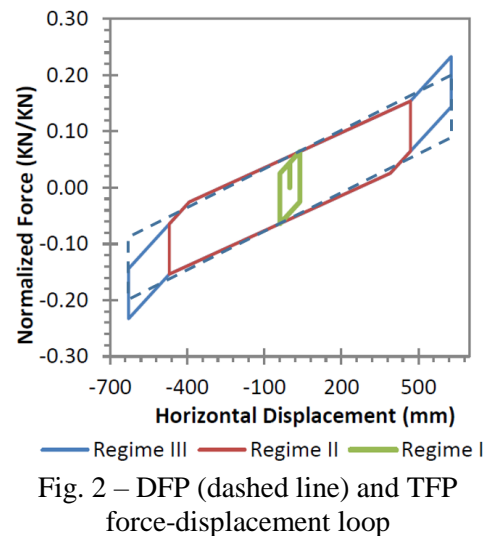
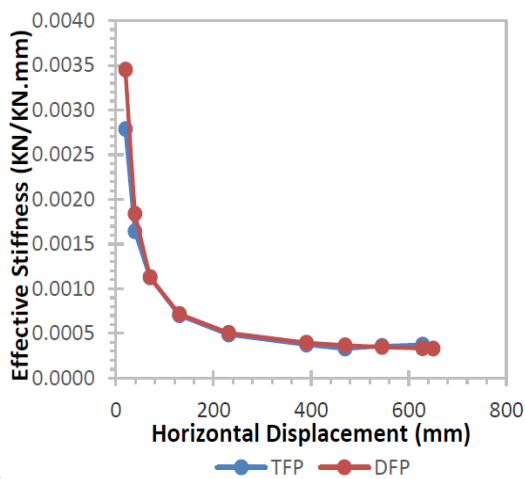
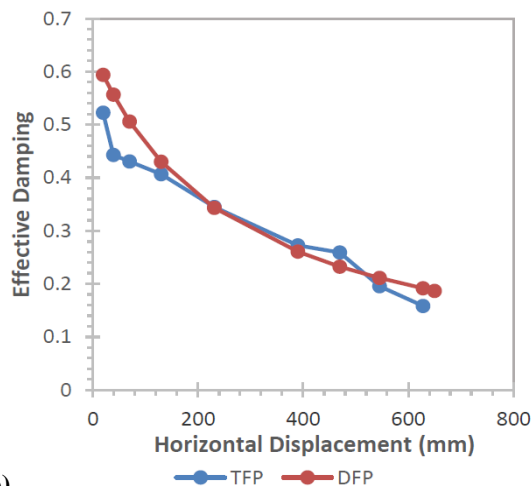


Fig. 2 – DFP (dashed line) and TFP force-displacement loop



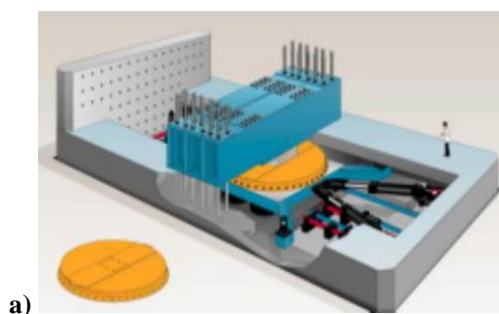
a)



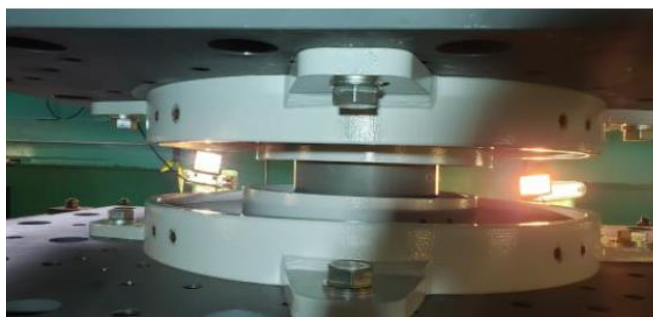
b)

Fig. 3 – Expected a) effective stiffness and b) damping ratio vs displacement for DFP and TFP devices

Shake table tests were performed at the UC San Diego Caltrans SRMD facility to verify the expected performance. The set-up includes the generation of vertical forces by pressing the isolator against a cross steel beam, and application of mono- and bi-directional displacement control motion in the horizontal direction. A sample testing setup overview and installment can be seen in Fig. 4.



a)



b)

Fig. 4 – Shake table a) testing setup, and b) TFP installment

The testing protocol is summarized in Table 2, and include mono-directional triangular and sine tests, and bi-directional cloverleaf and circular displacement tests.



Table. 2 – Testing protocol

Test #	Test type	Main DOF	Disp (mm)	Vert load (kN)	Freq (Hz)	Velocity (mm/s)	Accel (g)	Cycles
1	Triangle	Long/ Vert	549.0	1550	1/1000	2.2	0.001	1
				7750				
2	Sine	Long	549.0	7750	0.05	172.5	0.006	3
3	Sine	Long	549.0	1550	0.05	172.5	0.006	3
4	Sine	Long	549.0	6200	0.05	172.5	0.006	3
5	Sine	Long	152.5	6200	0.05	47.9	0.002	3
6	Sine	Long	305.0	6200	0.05	95.8	0.003	3
7	Sine	Long	457.5	6200	0.05	143.7	0.005	3
8	Clover Leaf (Longitudinal)	Long	549.0	6200	0.2	689.9	0.088	2
9	Clover Leaf (Lateral)	Lat	274.5	6200	0.2	344.9	0.044	2
10	Clover Leaf (Bi-Directional)	Long/ Lat	549.0	6200	0.2	689.9	0.088	2
11	Circular (Longitudinal)	Long	549.0	6200	0.2	689.9	0.088	2
12	Circular (Lateral)	Lat	549.0	6200	0.2	689.9	0.088	2
13	Circular (Bi-Directional)	Long/ Lat	549.0	6200	0.2	689.9	0.088	2

Mono-directional tests were used to verify the expected performance in terms of effective properties. The results are summarized in the following Figs. 5 and 6, which show a comparison between experimental and predicted analytical values for effective stiffness and damping ratio, respectively. Tests show that differences in effective stiffness are limited, while the difference in effective damping can be significant. These differences are mainly due by variations of the coefficient of friction during the sliding motion, associated with changes in the contact pressure and velocity, and generated heat. The TFP isolator presented damping ratio values that were consistently lower than expected values.

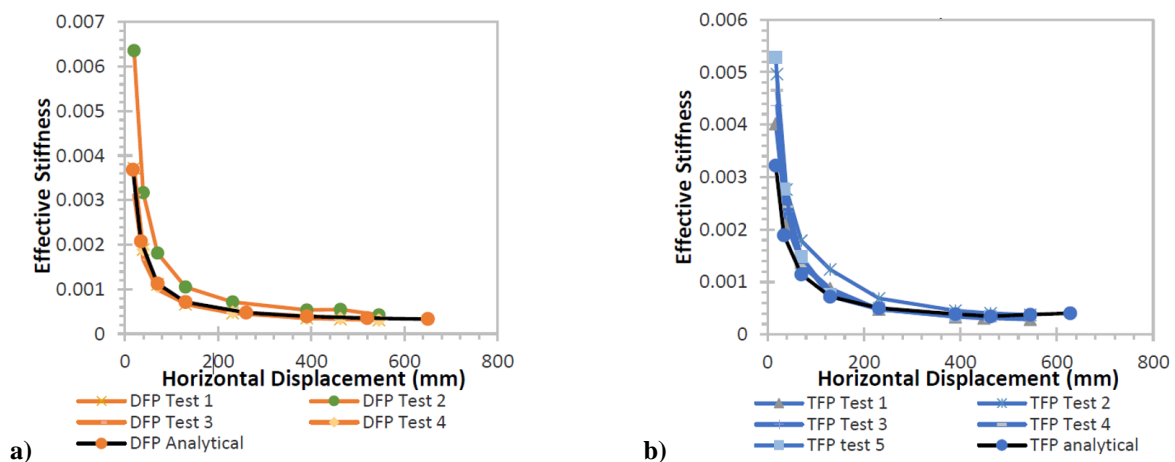


Fig. 5 – Experimental and analytical effective stiffness, for a) DFP and b) TFP devices

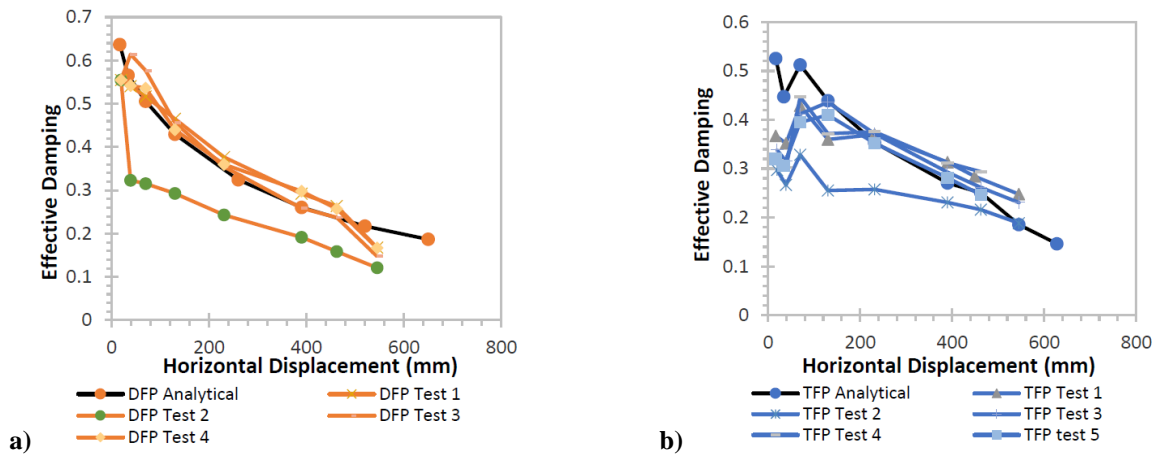


Fig. 6 – Experimental and analytical effective damping ratio, for a) DFP and b) TFP devices

The two devices also experience different vertical behavior, as shown in Fig. 7. The vertical displacement motion of the TFP reflects the change in curvature during different sliding regimes, resulting in sudden changes at the beginning and the end of the displacement loop. The complex vertical motion of the TFP device, if neglected in modeling the isolator, has the potential of generating unexpected and sudden vertical acceleration, which suggests the need for further investigation.

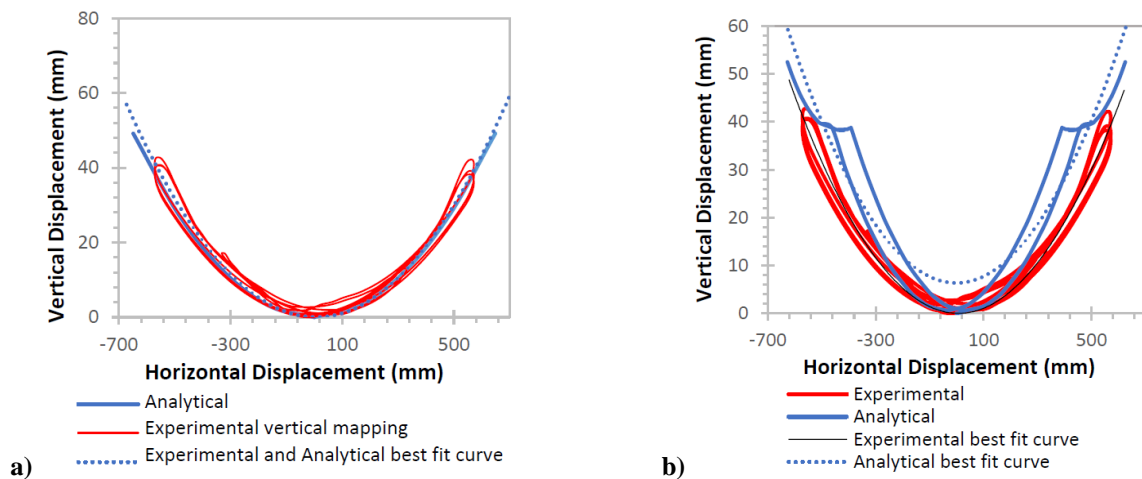


Fig. 7 – Experimental and analytical vertical displacement path, for a) DFP and b) TFP devices

The bi-directional clover-leaf and circular tests were performed as a basis for the calibration of the bi-directional model of the isolators, presented in the next section.

3. Analytical Model

The proposed analytical bi-directional equation of motion for the TFP is an extension of an existing DFP model [6]. In this model, the friction and restoring force terms that contribute to the lateral resistance of the isolator are identified as separate forces acting in variable directions. As with any non-colinear vector forces, these cannot be summed without regard for the difference in direction. The model incorporates unit vectors, as shown in Eq. (1), to account for the difference in directions of those terms:

$$F = \frac{N|u|}{R_{eff}} * \left\langle \frac{u}{|u|} \right\rangle + \mu N * \left\langle \frac{u'}{|u'|} \right\rangle \quad (1)$$



where F is the lateral force during sliding conditions, R_{eff} is the effective radius of curvature of the isolator, u is the displacement vector, u' is the time derivative of u (velocity vector), $N \geq 0$ is the compressive vertical force, and μ is the coefficient of friction, which could be affected by load, velocity, and cycling effects, as shown in [7].

Similarly, the TFP's behavior has equations of motion equal to the number of regimes that it can experience. The three aforementioned regimes that this TFP experiences are shown in Table 3 below as Eq. (2), (3), and (4). The subscripts 1 and 2 refer to sliding on the external and internal surfaces, respectively. Table 4 displays Eq. (5), (6), and (7) which describe the force of either the DFP or TFP for any load direction. The DFP equation is simply obtained by setting $\mu_2 \rightarrow \infty$. The displacement $d_i^* = d_i R_{i,eff} / R_i$ is the adjusted maximum displacement, based on the maximum sliding displacement d_i on each sliding surface. Fig. 8 displays the two forces (restoring and friction) acting in different directions during all regimes. The forces act on the surface that is in motion, the figure shows these forces switching between surfaces during motion. Specifically, the restoring force pulls towards the center of internal or external sliding surfaces, depending on the active regime, while the friction force is always tangent to the displacement path.

Table 3 – Mono-directional equations of motion

Regime	Exact Equation	Displacement Range	Displacement Equation
I	$F = \frac{N}{2R_{2,eff}} u + \mu_2 N$	$0 \leq u \leq u^*$	$u^* = 2(\mu_1 - \mu_2)R_{2,eff} \quad (2)$
II	$F = \frac{N}{2R_{1,eff}} (u - u^*) + \mu_1 N$	$u^* \leq u \leq u^{**}$	$u^{**} = u^* + 2d_1^* \quad (3)$
III	$F = \frac{N}{2R_{2,eff}} (u - u^{**}) + \frac{N}{2R_{1,eff}} (u^{**} - u^*) + \mu_1 N$	$u^{**} \leq u \leq u_{cap}$	$u_{cap} = 2d_1^* + 2d_2^* \quad (4)$

Table 4 – Bi-directional TFP equations of motion

Regime	Exact Equation
I	$F = \frac{W}{2R_{2,eff}} (u_2) * < \frac{u_2}{ u_2 } > + \mu_2 W * < \frac{u'}{ u' } > \quad (5)$
II	$F = \frac{W}{2R_{1,eff}} (u_1) * < \frac{u_1}{ u_1 } > + \mu_1 W * < \frac{u'}{ u' } > \text{ with } u_1 = u - u_2^* \quad (6)$
III	$F = \left(\frac{W}{2R_{2,eff}} (u_2) * < \frac{u_2}{ u_2 } > + \frac{W}{2R_{1,eff}} (2d_1^*) * < \frac{u_1}{ u_1 } > + \mu_2 W * < \frac{u'}{ u' } > \text{ with } u_2 = u - u_1 \text{ and } u_1 = 2d_1^* \quad (7)$

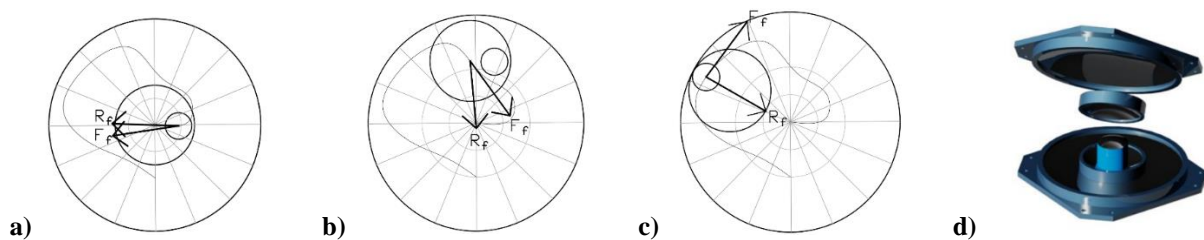


Fig. 8 – Direction of forces in a) Regime I, b) Regime II, c) Regime III; (d) TFP 3D surfaces

As previously mentioned, the proposed model was validated using experimental data. Fig. 9 displays sample comparisons between analytical and test data for sine, cloverleaf, and circular tests. Fig. 9a refers to a



mono-directional sine test, while Figs. 9b and 9c show the longitudinal and force-displacement loop obtained from the cloverleaf and circular bi-directional tests, respectively.

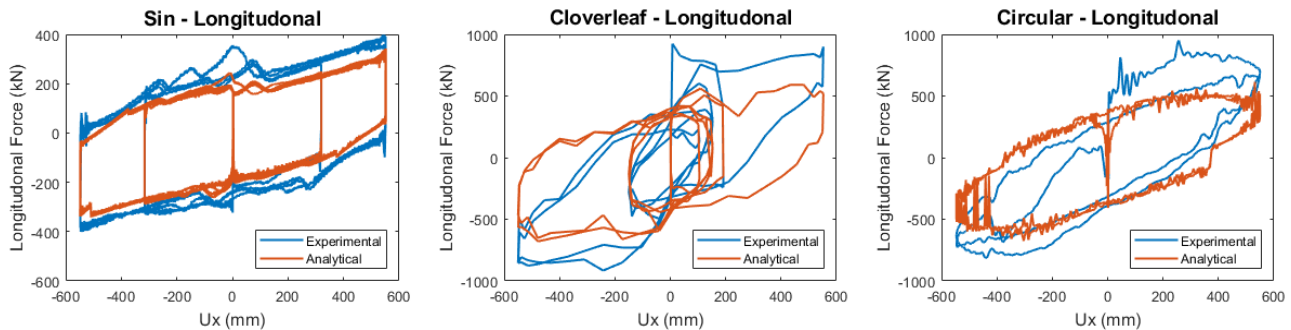


Fig. 9 – Sin sweep test 4 (left), Cloverleaf test 10 (center), Circular test 13 (right)

The proposed general formulation encompasses all loading combinations, and closely capture the mono-directional force-displacement loops, while shows a reduced stiffness in the bi-directional tests. This might be due to simultaneous sliding happening on inner and outer surfaces, which is not described by the model. This additional sliding motion is confirmed by the external sliding colliding with the edge of the isolator, which happened in both bi-directional tests. The effect of the collision is displayed clearly in Fig. 9c, where the force vibrates significantly throughout the displacement path.

It is also noticeable a difference between regimes between mono- and bi-directional tests of Fig. 9. The mono-directional test of Fig. 9a depicts clear changes between regimes, while the transition is not as noticeable in the bi-directional tests of Figs. 9b and 9c. Even in the mono-directional tests, there are discrepancies between analytical and experimental data, as the analytical model, after reversing motion, shows the isolator consistently re-entering regime II sooner than the experimental testing. A numerical analysis has been performed in order to investigate the kinematics of the model in better detail and to verify the feasibility of current commercial numerical models.

4. Detailed numerical model of TFP

The detailed numerical model of the TFP device was implemented in ABAQUS ®. It has dimensions and properties shown in Table 2 that match those of the experimentally tested TFP. The isolator is made of solid elements, and rigid contact with friction is used at the sliding surfaces. To replicate testing conditions, the isolator is with a fully fixed top slider (R_4) and a rotationally fixed bottom slider (R_1). The movement of the isolator is displacement controlled by a point at the centroid of the bottom slider. Resulting forces from displacement are evaluated at the fixed supports on the top surface. The isolator is shown in Fig. 10. For future studies, the model could be extended to account for the load, velocity, and cycling effects on the coefficient of friction.

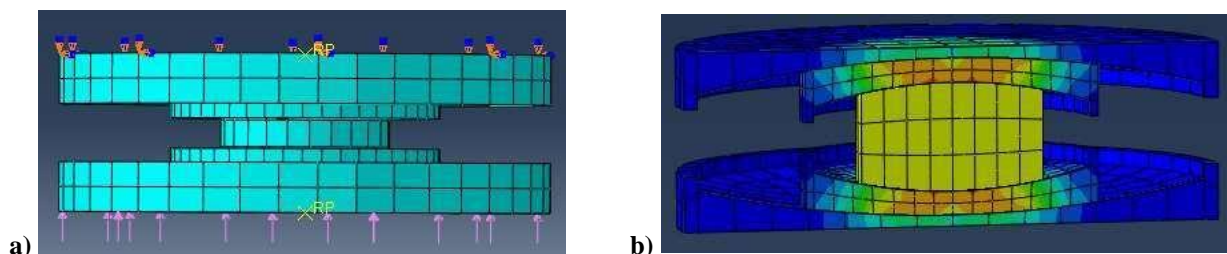


Fig. 10 – ABAQUS TFP a) model, and b) section view

The FEA model was able to reasonably predict experimental force-displacement results for various mono- and bi-directional tests. The numerical and experimental results are compared for the sine, cloverleaf, and circular displacements in Fig. 11, 12, and 13. The numerical results for the mono-directional sine displacement of Fig. 11 closely match the overall general behavior of the experimental results. Differences



occur where the numerical model slightly under predicts forces at the turning points due to not fully capturing the breakaway effect. Other differences are seen where the regime change to the outside surfaces occurs at a slightly different displacement in the numerical results compared to experimental.

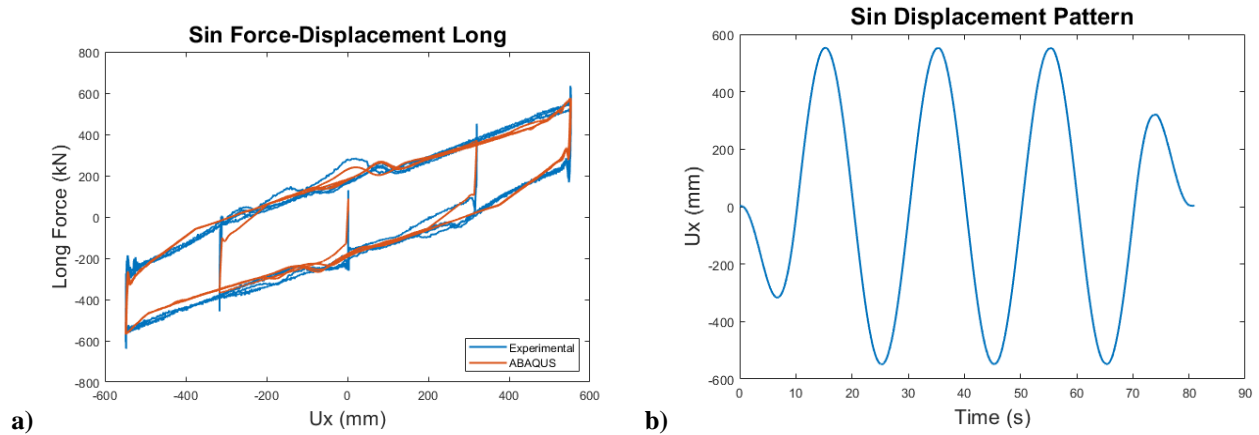


Fig. 11 – Sine a) force-displacement loop and b) displacement pattern

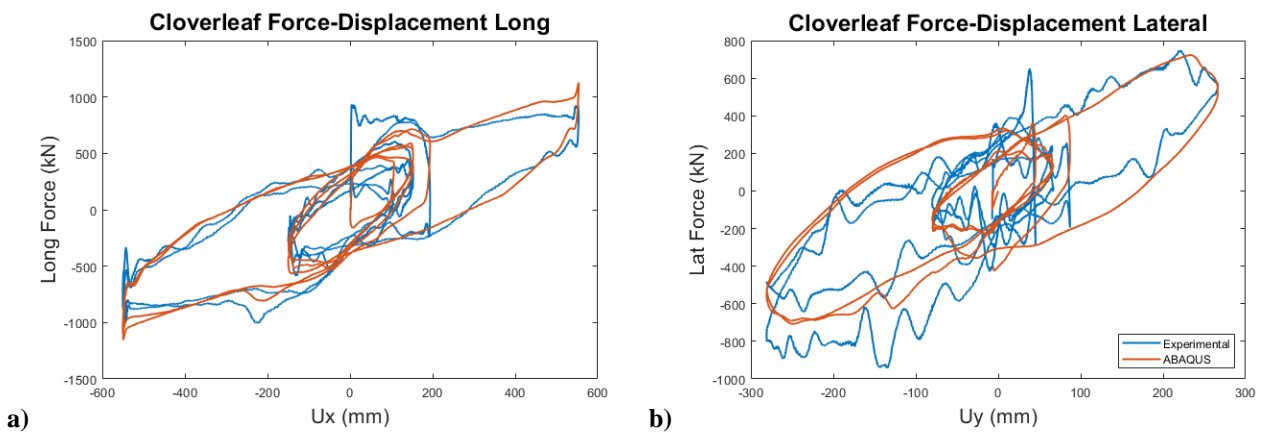


Fig. 12 – Cloverleaf force-displacement loop, longitudinal (left) lateral (right)

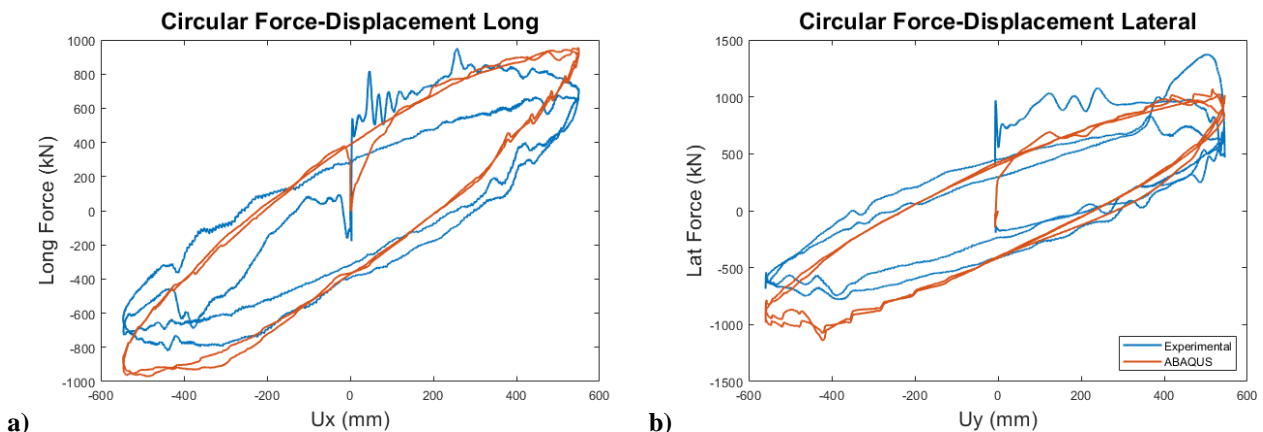


Fig. 13 – Circular force-displacement loop: a) longitudinal, and b) lateral

In the bi-directional cloverleaf test of Fig. 12, comparisons are made for both longitudinal and lateral displacements. In the longitudinal direction, numerical and experimental results closely coincide. Minor differences occur where the numerical model is too smooth and unable to capture the fluctuations in force as the isolator displaces. The numerical results also do not capture the large increase in force as the isolator was



first displaced from the rest. In the lateral direction, the general behavior is also well predicted, however, large fluctuations are seen in the experimental loop that was not captured numerically. This is due to residual vibrations from the isolator impacting the edge at the maximum displacement during the experimental testing.

Bi-directional results from the circular test of Fig. 13 also indicates accurate prediction from the numerical model. Both longitudinal and lateral behavior are well predicted for most of the loop, however discrepancies occur where the experimental test overly displaced and the isolator was damaged. This is visualized in the large increase in forces on the right side of the loops.

5. Numerical analysis of an isolated moment-resisting frame

A regular reinforced concrete moment-frame structure is used as a case study to evaluate the performance of TFP on structures. The structure has 4 stories at 3m, and 2 bays of 5m length in both longitudinal and lateral direction. Rigid diaphragms simulate the in-plane stiffness of the floor slabs. Rectangular (300x500mm²) floor beams are supported by a total of nine square (400x400 mm²) columns. Nine identical TFP isolators previously verified are located underneath each column. The total seismic weight of each floor, including seismic loads, is 1000kN, resulting in a cumulative weight of the whole building of 5160 kN [8]. The model was implemented in ABAQUS and in SAP2000, to perform a comparison between a detailed model and a lumped model, typically used for industry applications. In ABAQUS, elastic beam elements were used for the structural frame and solid elements for the isolators as shown in Fig. 14.

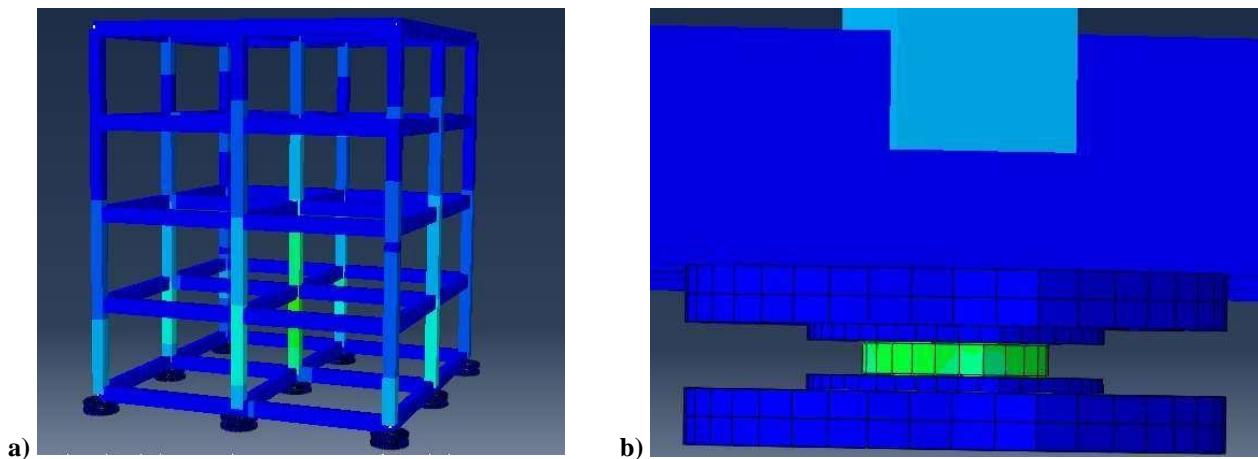


Fig. 14 – ABAQUS a) building model, and b) typical TFP

Full dynamic seismic nonlinear analyses were used to evaluate the structure under three different accelerograms shown in Table 5. Mono- (longitudinal only, case X), bi- (longitudinal and lateral, case XY), and tri-directional (longitudinal, lateral, and vertical, case XYZ) input components were considered for each ground motion, in order to investigate the differences between single- and multi-directional excitations. For modeling, the accelerations from earthquake ground motion were converted to X, Y, and Z component forces acting on the center of mass of each floor.

Table 5 – Earthquake Characteristics

Name	Year	Earthquake	Mw	Mech.*	Station	Site	PGA (g)	PGV (cm/s)	PGD (cm)
LP	1989	Loma Prieta	7.0	OB	LGPC	Soil	0.56	94.8	41.1
KO	1995	Kobe	6.9	SS	KJMA	Stiff Soil	0.82	81.6	17.7
ER	1992	Erzincan	6.7	SS	Erzincan	Soil	0.50	64.3	21.9



Force-displacement loops of the isolators are shown to be significantly affected by the inclusion of all components of tri-dimensional excitations. In Fig 15, longitudinal force-displacement loops of the center isolator are presented for the Loma Prieta earthquake along with the tri-directional XYZ excitation. Differences are seen in the prediction of peak displacement, peak force, and overall shape of the loops.

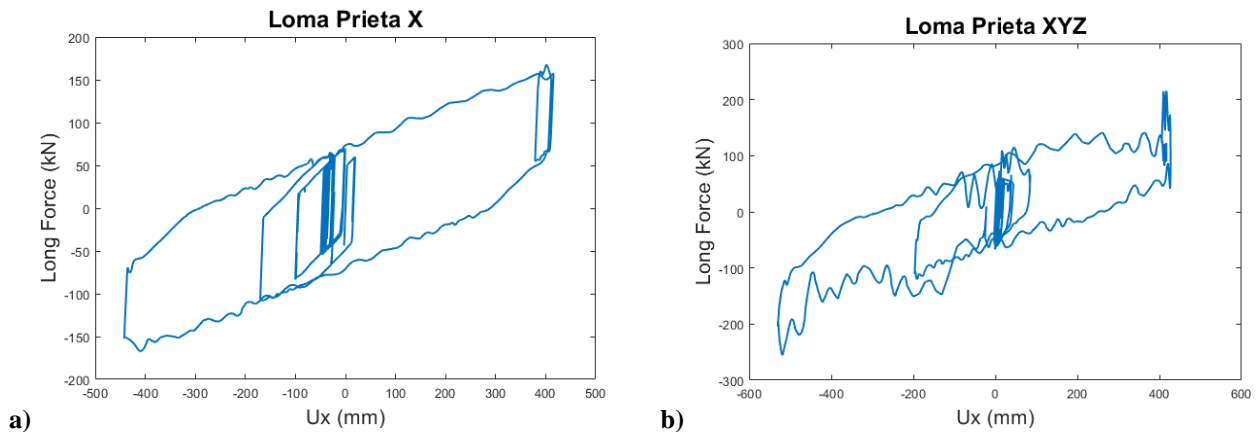


Fig. 15 – ABAQUS force-displacement loops of center isolator for Loma Prieta case a) X, and b) XYZ

The same 4-story reinforced concrete moment-frame previously analyzed was modeled in SAP2000 using the built-in Triple Friction Pendulum Link. A full dynamic non-linear analysis was performed for the X, XY, and XYZ cases of all 3 earthquakes. Displacements, isolator forces, and base shears were extracted from the model and compared to the detailed ABAQUS model in order to investigate the link behavior.

The SAP2000 resulting force-displacement loops for the center isolator from the Loma Prieta X and XYZ excitations are overlaid on the ABAQUS loops and shown in Fig. 16. It is seen in the Loma Prieta X case (Fig. 16a) that the behavior of the isolator appears to generally match theoretical behavior, but with some discrepancies. For a TFP with the coefficient of friction on both inside surfaces being the same and both outside surfaces being the same, it is expected to see a distinct shift in stiffness as the sliders on the outside surfaces contact the restrainer and sliding continues on the inside surfaces. However, the SAP2000 displacement loops show a gradual change in stiffness throughout the displacement, with no clear change in regime. The force-displacement loop has smooth lines and is not capturing fluctuations in forces, which were also observed in the experimental testing. Overall the SAP2000 results underestimate both displacement and forces as seen in the ABAQUS model. The SAP2000 loop for the Loma Prieta XYZ case (Fig. 16b) shows very similar behavior to the X case, which is not expected with the inclusion of the Z component. There is no fluctuation in forces with the vertical excitation, and the TFP link fails in capturing the increased peak displacement and force observed in the ABAQUS model.

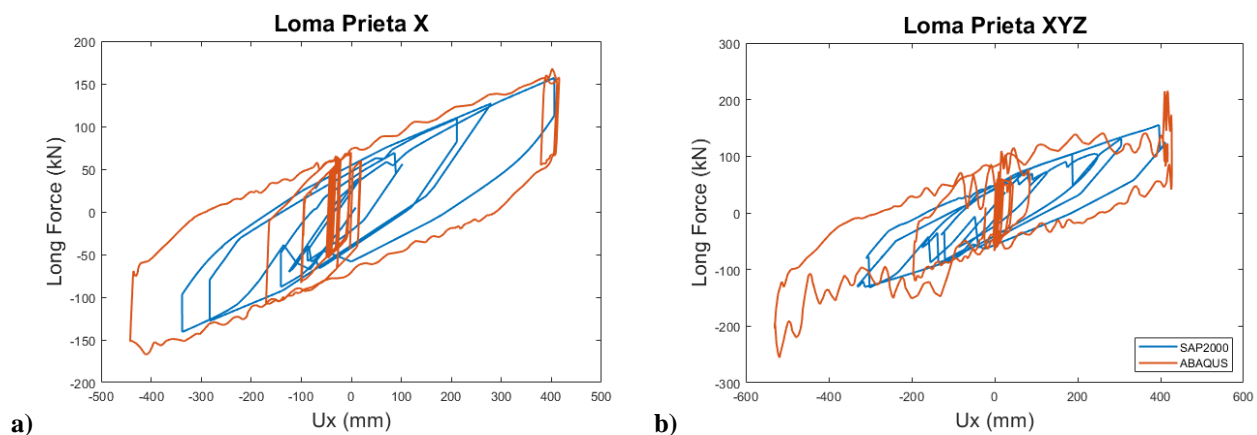


Fig. 16 –Center isolator force-displacement loops for Loma Prieta case a) X and b) XYZ



Peak displacements, isolator forces, and base shear values predicted by both models for X, XY, and XYZ load cases are summarized in Table 6. The largest difference is observed in peak displacements, with an average difference of 36.7%. SAP2000 both over- and under-predicted the ABAQUS displacements, with the largest difference being an overprediction of 80.3% in the Kobe X excitation. Over and underpredictions were also seen in peak isolator forces, where on average it differed by 13.2% with a maximum underprediction of 39.6% in the Loma Prieta XYZ excitation. Peak base shears were predicted with an average difference of 14.3%, and a maximum difference of 29.8% overprediction in the Kobe X excitation.

Table 6 – Isolated moment frame peak displacements, forces, and base shears

EQ	Peak Displacement (mm)			Peak Force (kN)			Peak Base Shear (kN)		
	Abaqus	SAP	Diff (%)	Abaqus	SAP	Diff (%)	Abaqus	SAP	Diff (%)
LP-X	442.11	405.84	-8.2	167.76	156.91	-6.5	816.39	853.06	4.5
LP-XY	502.24	416.75	-17.0	182.27	154.90	-15.0	877.97	830.70	-5.4
LP-XYZ	533.90	413.91	-22.5	257.32	155.35	-39.6	1128.1	810.60	-28.1
Kobe-X	121.92	219.84	80.3	97.24	107.16	10.2	461.63	599.30	29.8
Kobe-XY	176.08	271.49	54.2	105.99	118.93	12.2	503.44	619.75	23.1
Kobe-XYZ	170.86	262.15	53.4	110.38	117.58	6.5	522.71	608.67	16.4
Erzincan-X	315.15	205.33	-34.8	140.53	108.67	-22.7	673.97	583.40	-13.4
Erzincan-XY	330.94	430.01	29.9	142.51	142.65	0.1	684.56	710.10	3.7
Erzincan-XYZ	332.45	433.26	30.3	142.98	151.06	5.7	700.87	731.72	4.4

Displacement histories of the two models are shown for the X excitation case of all earthquakes in Fig. 17. Large discrepancies in the analysis are clearly visible. The most noticeable differences consist in an early sliding of the SAP2000 model, followed by an increased number of oscillations. This is consistent with the narrower shape of the force-displacement loops of Fig. 16, which result in lower friction forces and reduced energy dissipation throughout the cycling.

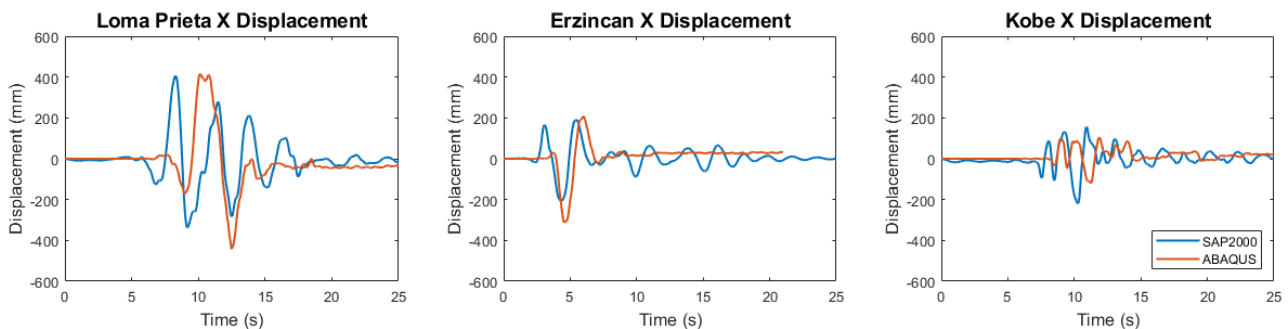


Fig. 17 – Displacement responses for SAP2000 isolated moment frame

6. Conclusion

Two supposedly equivalent DFP and TFP seismic isolation devices were investigated, with the aim of experimentally verify their performance. The devices have been designed to have the same effective stiffness and damping properties at the design displacement level. The analytical formulas used to design and predict the performance of the devices were able to capture the variability of the effective stiffness with the displacement for both devices. Experimental results, however, showed that analytical formulas tend to overestimate the TFP energy damping performance, mostly due to the experimentally observed variability of the friction performance, which inevitably affects the kinematics of the device.



A unified analytical model was proposed to predict the performance of DFP and TFP devices. The model is an extension of a previously defined DFP model and uses unit vectors to identify the direction of friction and restoring force components during different sliding regimes of the TFP device. The results from the new derivations showed the model's ability to capture the behavior described by mono-directional equations of motion. The model is also able to capture the overall bi-directional behavior of such seismic isolators. However, discrepancies were observed between the experimental and analytical force-displacement loops, which were mainly attributed to effects not accounted for in this study, such as the friction performance variability.

A full dynamic nonlinear analysis was finally performed to verify the kinematic of the TFP isolator and calibrate a detailed numerical model. The detailed isolator model was used to predict the behavior of an isolated moment-resisting frame structure, subjected to three multi-directional excitations seismic. A dynamic nonlinear analysis was performed with the detailed numerical model and a lumped link model that represents current industry state-of-practice. Results showed that the lumped isolator model can predict the general behavior of a triple friction pendulum, but does not accurately capture regime changes, fluctuations in forces due to vertical component, and overall has clearly defined force-displacement loops that are not representative of experimental observations, particularly for bi-directional excitations. This results in significant differences in the overall behavior between the lumped and the experimentally calibrated detailed model. Large discrepancies in the isolated building performance were observed in terms of maximum displacements (80.3%), isolator forces (39.6%), and base shears (29.8%). The inconsistency results in over-prediction and under-prediction of structural demand parameters, depending on the seismic excitation. This inconsistency suggests the need for more sophisticated models, which could fully capture the seismic performance of such devices.

7. References

- [1] Morgan, T. A., & Mahin, S. A. (2010): Achieving reliable seismic performance enhancement using multi-stage friction pendulum isolators. *Earthquake Engineering & Structural Dynamics*, **39** (13), 1443-1461.
- [2] Fenz, D. M., Constantinou, M. C. (2008): Modeling triple friction pendulum bearings for response-history analysis. *Earthquake Spectra*, **24** (4), 1011-1028.
- [3] Sarlis, A. A., Constantinou, M. C. (2016). A model of triple friction pendulum bearing for general geometric and frictional parameters. *Earthquake Engineering & Structural Dynamics*, **45** (11), 1837-1853.
- [4] Giammona, A. P., Ryan, K. L., & Dao, N. D. (2015): Evaluation of assumptions used in engineering practice to model buildings isolated with triple pendulum isolators in SAP2000. *Earthquake Spectra*, **31** (2), 637-660.
- [5] Becker, T. C., & Mahin, S. A. (2012): Experimental and analytical study of the bi - directional behavior of the triple friction pendulum isolator. *Earthquake engineering & structural dynamics*, **41** (3), 355-373.
- [6] Lomiento, G., Bonessio, N., & Benzoni, G. (2013). Concave sliding isolator's performance under multi-directional excitation. *Ingegneria Sismica*, **30** (3), 17-32.
- [7] Lomiento, G., Bonessio, N., & Benzoni, G. (2013): Friction model for sliding bearings under seismic excitation. *Journal of Earthquake Engineering*, **17** (8), 1162-1191.
- [8] Lomiento, G., Bonessio, N., Ökten, M. S., & Benzoni, G. (2015): Effect of frictional characteristics on the response of sliding base-isolated buildings under three components of earthquake excitation. In *Proc. 14th World Conference on Seismic Isolation, Energy Dissipation and Active Vibration Control of Structures*.